

Article

Writing Tiny Nanoclusters Using a Nanofountain Pen Operated by Spontaneous Evaporation

Sung-Jo Kim ^{1,†}, Dongwon Yi ^{2,†}, Il Hyun Lee ^{3,4,5}, Won-Geun Kim ⁶, Ye-Ji Kim ³, Jong-Sik Moon ^{7,*}
and Jin-Woo Oh ^{1,3,8,*} 

¹ BIT Fusion Technology Center, Pusan National University, Busan 46241, Republic of Korea; sungjokim84@pusan.ac.kr

² Division of Endocrinology and Metabolism, Department of Internal Medicine, Pusan National University Yangsan Hospital, School of Medicine, Pusan National University, Yangsan 50612, Republic of Korea; drwonny@pusan.ac.kr

³ Department of Nano Fusion Technology, Pusan National University, Busan 46241, Republic of Korea; 2023710262@skku.edu (I.H.L.); kyeaj0153@pusan.ac.kr (Y.-J.K.)

⁴ Department of Nano Engineering, SKKU Advanced Institute of Nanotechnology (SAINT), Sungkyunkwan University (SKKU), Suwon 16419, Republic of Korea

⁵ Department of Nano Science and Technology, SKKU Advanced Institute of Nanotechnology (SAINT), Sungkyunkwan University (SKKU), Suwon 16419, Republic of Korea

⁶ Department of Mechanical Engineering, Pohang University of Science and Technology (POSTECH), Pohang 37673, Republic of Korea; kim1guen@postech.ac.kr

⁷ School of Fire Safety, Kyungil University, Gyeongsan 38428, Republic of Korea

⁸ Department of Nano Energy Engineering, Pusan National University, Busan 46241, Republic of Korea

* Correspondence: jsmoon@kiu.kr (J.-S.M.); ojw@pusan.ac.kr (J.-W.O.)

† These authors contributed equally to this work.

Abstract: Two-dimensional and 3-dimensional colloidal structures have been used to study surface-enhanced Raman scattering and localized surface plasmon resonance because of their regular stacking structures. However, freely controlling the number and size of the colloidal assemblies remains a challenge. In this study, we demonstrated the fabrication and mechanism of tiny nanoclusters using spontaneous evaporation-based nanofountain pens (NFPs). A micrometer-scale NFP nozzle was fabricated using a glass capillary. The gold nanoparticles (AuNPs) dispersed ink formed the pendant droplet at the NFP nozzle tip, where the AuNPs accumulated within the pendant droplet because of evaporation. The accumulated AuNPs were transferred onto the substrate via a stamp-like process to create nanoclusters. Using water evaporation analyzed by diffusion equations, we showed that reducing the AuNP accumulation to one hundred is possible. This precise adjustment enables fabrication until submicrometer-level nanoclusters. The fabrication method using NFPs can create 3D structures, and this operation is not significantly affected by the size or composition of the AuNPs. This could be expanded to metabolite-included nanocluster where metabolite can be located at the hot spot among AuNPs. Therefore, we expect that this will be utilized to create SERS signals and conduct disease diagnosis research using extremely small amounts of metabolites.

Keywords: colloidal assembly; nanocluster; gold nanoparticle; nanofountain pen; evaporation; capillary action



Citation: Kim, S.-J.; Yi, D.; Lee, I.H.; Kim, W.-G.; Kim, Y.-J.; Moon, J.-S.; Oh, J.-W. Writing Tiny Nanoclusters Using a Nanofountain Pen Operated by Spontaneous Evaporation. *Crystals* **2024**, *14*, 9. <https://doi.org/10.3390/cryst14010009>

Academic Editors: Abdur Rauf and Mujeeb Ur Rehman

Received: 21 November 2023

Revised: 15 December 2023

Accepted: 20 December 2023

Published: 21 December 2023



Copyright: © 2023 by the authors. Licensee MDPI, Basel, Switzerland. This article is an open access article distributed under the terms and conditions of the Creative Commons Attribution (CC BY) license (<https://creativecommons.org/licenses/by/4.0/>).

1. Introduction

The potential applications of localized surface plasmon resonance (LSPR) for small objects on the nanometer scale require significant attention [1–5]. When light enters subwavelength-scale metallic nanoparticles, the nanocluster exhibits LSPR, which can be used for practical purposes with a wide optical range such as biosensors [4–6], energy devices [7–9], chemical synthesis [10–12] and surface-enhanced Raman spectroscopy [13–15]. To realize the production of high-performance functional optical devices, it is essential

possess the capability to both design and manipulate LSPRs. One plausible method to achieve this may be by manipulating plasmon resonance using self-assembly of nanoparticles (NPs) [16,17]. Heightened radiative damping leads to spectral broadening when dipolar plasmons across all nanoparticles oscillate coherently. Conversely, out-of-plane oscillations reduce radiative damping, resulting in a spectral dip. The ensemble of plasmon modes changes according to the NP clusters and determines the LSPR properties. The plasmon modes of NP clusters can be tuned depending on the shape, size, dielectric perimeter, and interparticle distance of the NPs, which opens up possibilities for sensor applications [16,17]. Recently, the enhancement and manipulation of LSPR by changing the geometric packing structures and composition of nanoclusters has also been demonstrated [18–21].

Lithography via top-down manufacturing has long been used to develop plasmonic structures [16,17,22,23]. Electron-beam or ion-beam lithography enables the creation of nanometer-sized metal objects by adjusting their geometry and gap distance. However, it is less cost-effective and has low throughput. In addition, the generated structures are limited to two dimensions, making it difficult to scale them into three dimensions when stacked vertically, but this difficulty can be overcome by introducing solution-processed self-assembly [24–26]. This method offers advantages such as simplicity, scalability, and high-throughput paths for constructing 2D and 3D plasmonic clusters. Marangoni flow induced by surface tension gradients owing to nonuniform evaporation contributes to the aggregation of NPs, forming dense clusters at two- or three-phase interfaces in solution-mediated mass transfer processes, such as dip coating [24]. The Langmuir–Brogett method and template-assisted self-organization have been designed [25,26]. Although several colloidal assembly technologies are being developed, constraints on creating free three-dimensional structures or changing the composition of plasmonic clusters composed of NPs are still difficult.

Nanocluster-based biosensors can be developed via LSPR or surface-enhanced Raman scattering (SERS). SERS is a non-destructive method that does not require sample preparation. This provides insight into the intrinsic molecular vibrations of metabolites and small molecule analytes in biological samples [27–31]. Enhancement of the electromagnetic field, achieved through LSPR excitation of nanostructured metal surfaces, increases the Raman signal by up to more than 10 times [32–36]. Additionally, nanogaps between two or more metal NPs containing dielectrics generate localized electromagnetic field enhancements (hot spots) by LSPR [37–39]. SERS has been studied for metabolome analysis with its high sensitivity and characteristic spectra [40–42]. However, since the area where electromagnetic waves are maximally enhanced is relatively small compared to the total area, the possibility of target substances infiltrating the area is low [43]. Additionally, the surface structure of typical SERS substrates may cause changes in Raman signals due to low reproducibility of size, distribution, and shape [44]. A process using a semiconductor process is being developed to ensure the reproducibility of structures and signals, but this method requires expensive equipment for the semiconductor process, and it is not easy to specify the location where the hot spot and the sample overlap. Therefore, achieving signal uniformity in SERS substrates for metabolomics and biosensing applications remains difficult [45,46]. To overcome these problems, the development of nanocluster manufacturing technology into which metabolites can be inserted is required.

In this study, we report a method for fabricating tiny nanoclusters using an NFP. To create a nanocluster, the NFP with a nozzle inner diameter of the order of micrometers was manufactured and filled with ink in which gold nanoparticles (AuNPs) were dispersed. The contact of the NFP nozzle was adjusted to produce nanoclusters using the movement of the substrate mounted on a finely adjusted motorized stage. The creation of nanoclusters is explained by solving the diffusion equations, and we make nanoclusters at the sub-micrometer level by adjusting the parameters related to the evaporation volume of the ink. By understanding the precise control of nanoclusters, one can more easily tackle the fabrication of nanoclusters containing target chemicals. Furthermore, we expect that these

structures will be widely used in detection studies through SERS- and LSPR-based optical signal generation and interpretation.

2. Materials and Methods

2.1. Preparation of Nanoparticles-Dispersed Ink

The ink used for nanocluster fabrication consisted of liquid water (dispersion medium) and AuNPs (dispersed phase). AuNPs were purchased from Nanocomposix (San Diego, CA, USA) and coated with polyvinylpyrrolidone (PVP) which makes the surface of AuNPs hydrophilic for homogeneous dispersion in water. The diameter (d) of the AuNPs was 77 ± 9 nm. We increased the concentration of ink by centrifugation with 14,500 RCF (Relative Centrifugal Force (RCF)) because the initial concentration of commercial AuNP solutions is too low for nanofountain pen (NFP)-based fabrication. The ink concentration was increased in the range of 0.5 to 5 mg/mL. The concentration (c in mg/mL) of the ink is then assigned as c_{ink} . The number density ($n = \frac{6c}{\pi d^3 \bar{\rho}}$) was also defined, where $\bar{\rho} = 19.32$ g/cm³ is the mass density of the AuNPs.

2.2. Preparing Micrometer-Sized Nozzle of NFPs

A micrometer-sized nozzle is necessary to fabricate nanoclusters of NFP since the mechanism worked by spontaneous evaporation is available in the micrometers range. A micropipette puller (P-97, Sutter Instruments, Novato, CA, USA) with a borosilicate glass capillary (ITEM No. 1B100F-6, outer diameter: 1.0 mm) was used to fabricate the nozzle. They were purchased from World Precision Instruments. The pulling conditions of the puller were set to 520–530 °C and 10–20 pulling velocities. The pulling velocity represents the separation rate of the puller bars when the capillary begins melting. The pulled and melted capillary transformed into an hourglass shape before breaking. The broken neck provides a micrometer-sized inner diameter of 5 μm at the velocity 10 and it reaches 1 μm -diameter at the velocity 20.

2.3. Fabrication Setup for Using NFPs

A motorized stage system was used because the precise position control of NFP is required to fabricate the nanoclusters. The NFP was equipped with a three-axis (xyz configuration) manual stage (PT3A/M; Thorlabs, Newton, NJ, USA). The substrate (silicon wafer) was mounted on a three-axis (xyz configuration) motorized stage with a backlash-free ballscrew, which controls the accurate position, and the DC motors (M-VP-25XA-XYZR, Newport, Irvine, CA, USA). The position of the substrate was carefully adjusted using a stage controller (XPS-D4, Newport, Irvine, CA, USA). To observe the fabrication process, a microscope was used to obtain a side view. A halogen lamp (OSL2, Thorlabs, Newton, NJ, USA) was used as the light source, and a 20 \times objective lens (MY20X-804, Mitutoyo, Kanagawa, Japan) was used to observe the fabrication process, and a charge-coupled device camera was used for real-time viewing and recording.

The initial nozzle position was set using a manual stage, where the distance between the nozzle and substrate was adjusted to approximately 100 μm . The contact and detachment processes were set using a stage controller that moved the substrate, and this discontinuous process was defined as a stamp-like process. This setting enabled us to touch the nozzle onto the substrate. The substrate motions of contact and detachment were set to a speed of 25 mm/s, and the contact time was 1 s in all the experiments. The time between detachment and contact was variable and defined as the accumulation time (t_A). The accumulation time and ink concentration governed the evaporation related to the accumulation of AuNPs at the nozzle tip.

2.4. Measurement of Nanocluster Structures

The shape and packing structure of the nanocluster was captured using scanning electron microscopy (SEM, JSM-7900F, JEOL Ltd., Tokyo, Japan). In addition, an atomic force microscope (AFM, NX10, Park Systems, Suwon, South Korea) was used to measure

the three-dimensional shape and volume of the nanoclusters in a noncontact mode using the data acquisition program XEP 3.0.4. The measured images were analyzed using the XEI 1.8.2 image processing program (Park Systems).

3. Results and Discussion

3.1. Nanoclusters Fabricated by a Nanofountain Pen

Understanding the manufacturing mechanism of nanoclusters can be used to design structures with optical properties such as SERS or LSPR. We seek to understand the mechanism through the fabrication of tiny nanoclusters using a NFP operated by spontaneous evaporation. An experimental setup equipped with a motorized stage must be used because the substrate mounted on the stage must move precisely at the micrometer-level scale Figure 1a). The NFP fixed to the holder was filled with ink in which AuNPs are dispersed to a height greater than 20 mm Figure 1b). The ink used in this study was adjusted to a number density (n) equivalent to approximately one AuNP (d , diameter of AuNP) contained in a cube with a side length (L) of 1 μm . SEM image shows AuNPs when the ink was dried on a glass substrate Figure 1c). The inner diameter ($2R$, R is the radius) of the nozzle tip of the NFP was adjusted to within the range of 1–5 μm Figure 1d). Fabricating tiny nanoclusters is possible by spontaneous evaporation using number-density and micrometer-level nozzles.

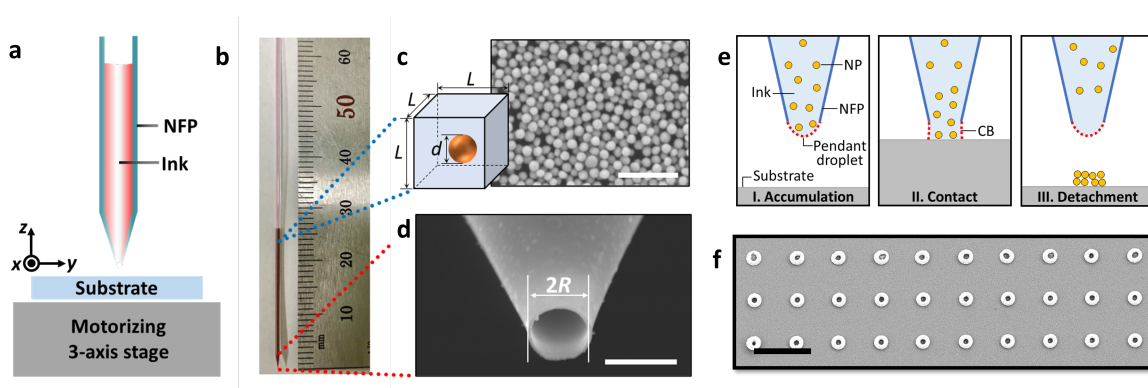


Figure 1. Fabrication of nanoclusters using a nanofountain pen (NFP). (a), Experimental setup for writing tiny nanoclusters utilizing the NFP. (b), NFP filled by gold nanoparticles (AuNPs)-dispersed ink. (c), SEM image of AuNPs. The scale bar represents 500 nm. (d), Nozzle of the NFP. The scale bar represents 5 μm . (e), Schematic of a stamp-like process consisting of (I) Accumulation, (II) Contact, and (III) Detachment. (f), Repeating the fabrication of half-donut-like nanoclusters. The scale bar represents 20 μm .

Tiny nanoclusters can be fabricated using NFP and stamp-like processes. This process consisted of three steps: (I) accumulation, (II) contact, and (III) detachment Figure 1e). During the accumulation step, the substrate mounted on the motorized stage remained at a distance of 100 μm from the nozzle tip of the NFP, and the water evaporation occurred at the pendant droplet during accumulation (t_A). Next, the substrate rose quickly and touched the pendant droplet hanging from the nozzle during the contact step. The pendant droplet then changed to a cylindrical shape, which is called a capillary bridge (CB). This contact was maintained for 1 s, after which the substrate quickly descended, the CB broke, and a pendant droplet was created at the end of the nozzle in the detachment step. The broken CB left the nanocluster after drying the water on the substrate. By combining this stamp-like process with the horizontal movement of a motorized stage, regularly repeating nanoclusters can be fabricated Figure 1f).

3.2. Structure Characteristics According to Fabrication Condition

The accumulation time and ink concentration are crucial to forming nanoclusters in the stamp-like process Figure 2a). One NFP was used for each ink concentration, and the change in the shape of the nanocluster was measured by changing the accumulation

time. This implies the images in one row in Figure 2a were produced using one NFP, and thus the inner diameter of the nozzle was not changed. The outermost diameter of the generated nanocluster matches the inner diameter of the NFP nozzle when the AuNP concentration in the ink was greater than 5 mg/mL. For the ink with an AuNP concentration of 1 mg/mL, the shape of the nanocluster was changed according to the accumulation time (e.g., $t_A = 10$ s for 1 mg/mL). When the accumulation time was short, traces larger than the inner diameter of the nozzle remained on the substrate. The outermost diameter of the created structure decreased and reached the inner diameter of the nozzle when the accumulation time increased. For $t_A = 5$ s at 1 mg/mL, it was difficult to confirm the structure of the nanocluster created through the stamp-like process. It should also be noted that nanoclusters are not created as marked by the green boxes when both the accumulation time and concentration increased. These results indicate that appropriate accumulation time and ink concentration conditions are required for nanocluster formation. We note that the nanocluster diameter is matched to the nozzle diameter used.

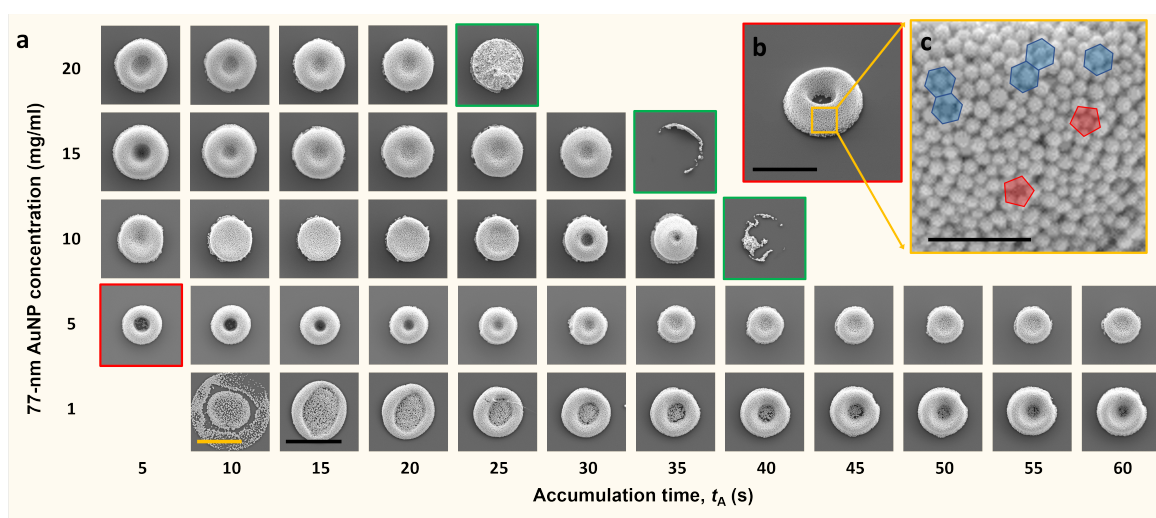


Figure 2. Structure changes of nanoclusters. (a), Shapes of nanoclusters regarding accumulation time and concentration. The yellow and black scale bars represent 5 μm , and other images follow the black scale bar. (b), SEM image of a half-donut-like nanocluster. This displays a tilted image marked red frame in Figure 2a, and the scale bar represents 3 μm . (c), Packing of gold nanoparticles (AuNPs). This shows a magnified image of Figure 2b, and the scale bar is 500 nm.

The nanoclusters exhibit a random, close-packed AuNP structure. Figure 2b shows an image of a nanocluster measured in an inclined state as marked in a red box of Figure 2a. There were no AuNPs near the center of the nanocluster, but AuNPs were piled up only in a circular band at the edge, similar to the shape of a half donut. The center of the half-donut-like nanocluster tends to fill gradually as the accumulation time of the stamp-like process increases. To confirm the packing structure, the surface of the half-donut-like nanocluster was enlarged Figure 2c). When measuring the number of first nearest neighbors surrounding a single AuNP, in most cases, it was surrounded by six AuNPs (marked by blue hexagons), and in rare cases, it was surrounded by five AuNPs (marked by red pentagons) [47]. Because the distance between the centers of the first nearest neighbors is equal to the diameter of the AuNPs, we can assume that the AuNPs consisting of nanocluster are random-close packed. Subsequently, the packing density or packing fraction (γ) is distributed in the range of 0.625–0.641 [48].

The morphological changes depended on the accumulation time in the accumulation step. The three-dimensional morphology of the nanocluster was measured using atomic force microscopy (AFM), as shown in Figure 3a where the 5 mg/mL of ink concentration was used for the fabrication. The AuNPs were stacked on a circular ring with a void at the center. The outermost diameter of the ring was the same as that of the NFP nozzle. Using

the height profile distributed on the xy plane, the center of mass (r_0) was calculated, and the radial profiles of the nanoclusters were estimated from each center, $r - r_0$ Figure 3b). For a short accumulation time (less than 20 s), the AuNPs were spread more on the substrate. However, the nanocluster formed well following the confinement of the nozzle when the accumulation time was over 20 s, and their shapes were similar. This result indicates that the nozzle size exhibited a confinement effect when the nanocluster was forming.

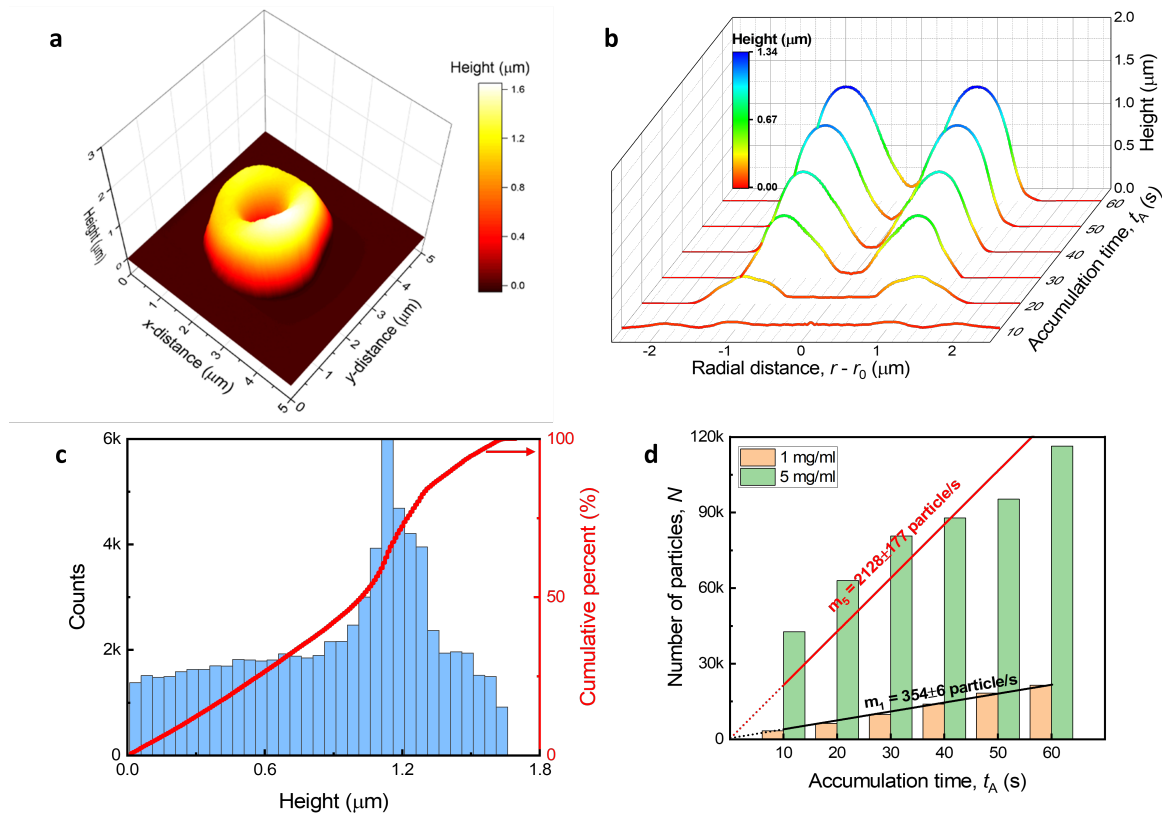


Figure 3. Morphology and volume of nanocluster. (a), Three-dimensional morphology. (b), Radial height profiles of half-donut-like nanoclusters. The color scale bar represents the height. (c), Height distribution of printed nanocluster. (d), Changes of stacking gold nanoparticles (AuNPs) regarding accumulation time and concentration.

The nanocluster volume depended on the accumulation time and ink concentration. To estimate the nanocluster volume, we investigated the height profiles of nanoclusters. The AFM image as shown in Figure 3a, one-pixel is $0.0015 \mu\text{m}^2$ in area. The height was counted using a bin size of 50 nm Figure 3c), and all pixels were included in counting as shown in the cumulative curve (red solid line). Using the height counts and area, the nanocluster volumes (V) were calculated and they exhibited the volume at the femtoliter level. The created structure was nanoporous as seen in Figure 2c, the volume occupied by AuNPs excluding voids (\tilde{V}) could be estimated by multiplying the calculated volume by the packing fraction (γ), which is expressed as $\tilde{V} = \gamma V$. The volume of an AuNP (v) with diameter d is expressed as $v = \frac{\pi d^3}{6}$; thus, the total stacking number of AuNPs consisting of the nanocluster is expressed as $N = \frac{\tilde{V}}{v}$. Notably, N increases according to the increment of t_A , and the 5 mg/mL concentration of ink exhibited higher stacking by approximately six times than 1 mg/mL of ink Figure 3d). This indicates that the stacking number ratios of $m_1 = 354 \pm 6$ and $m_5 = 2128 \pm 177$ particles/s can be adjusted using NFP. The subscript of the stacking number ratio represents the ink concentration (c_{onk}) for 1 and 5 mg/mL, respectively.

3.3. Spontaneous Evaporation-Driven Fabrication Mechanism

The nanofountain pen (NFP) operates via an exceptional balance between water evaporation and capillary action. To understand the operating principles of the NFP, we investigated the phenomena occurring at each step in the stamp-like process. The first factor considered was the height of the ink filled into the NFP. We empirically found that if the NFP was not filled with sufficient ink, the AuNPs would not be transferred to the substrate, even if the stamp-like process was repeated. Therefore, the ink at the tip of the nozzle did not come into contact with the substrate during the contact process. However, when the ink was sufficiently filled, the structure could be easily created using a stamp-like process. The forces acting on the ink within the capillary tube were studied to understand this phenomenon. As shown in Figure 4a, the cylindrical body (inner radius R_1) of NFP is filled with ink, and it is ejected through a nozzle tip (inner radius R_2). We note that the R_1 is in the millimeter range and R_2 is in the micrometer range. When ink is filled to the height H in the NFP, it experiences capillary forces ($F_1 = \pi R_1^2 \times \frac{2\gamma \cos \theta}{R_1}$ and $F_2 = \pi R_2^2 \times \frac{2\gamma \cos \theta}{R_2}$) owing to the Young-Laplace pressure in the up (marked in yellow arrow) and down (marked in red arrow) directions, respectively. Here, $\sigma = 72$ mN/m is the surface tension of water [49], and θ is the contact angle of water at the water-glass-air interface [50,51]. In addition, the ink experiences $F_3 \approx \pi R_1^2 H \rho g$ because of the gravity (marked in blue arrow). Here, $g = 9.8$ m/s² is the gravitational acceleration and $\rho = 1$ g/cm³ is the mass density of water.

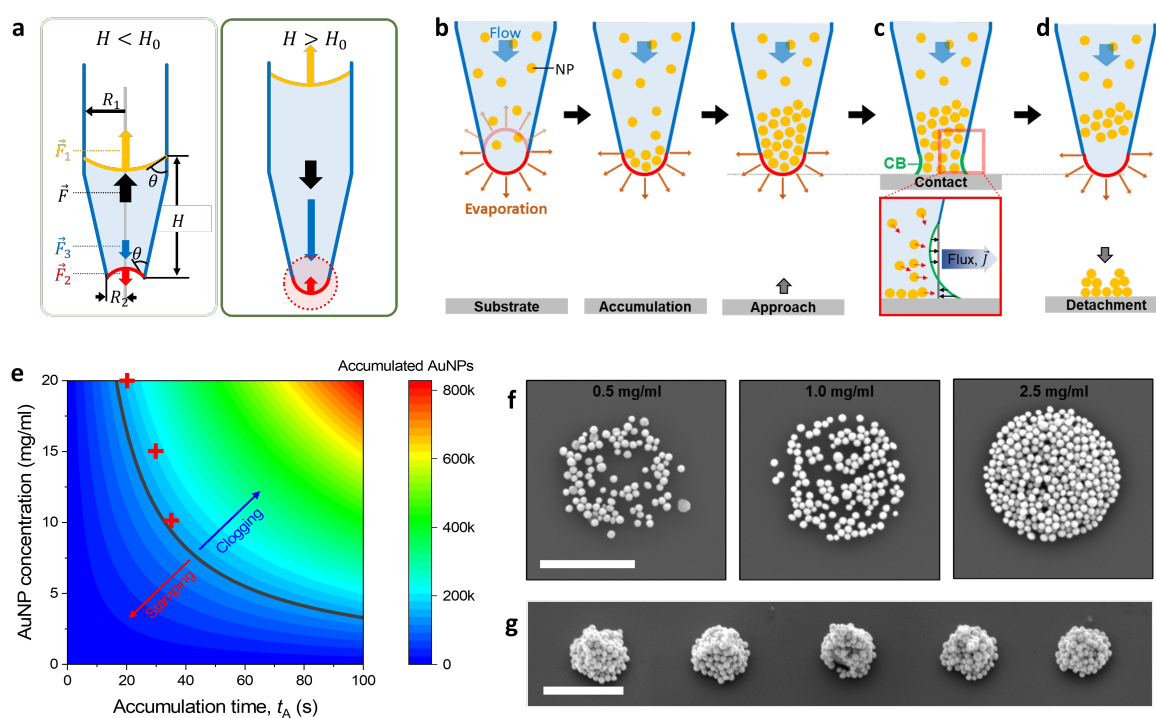


Figure 4. Fabrication mechanism of nanofountain pen (NFP). (a), Critical height of ink filled in the NFP for easy contact. (b), Accumulation of AuNPs based on the evaporation at the nozzle tip. (c), Transfer of AuNPs in the contact step. (d), Formation of nanoclusters after the detachment step. (e), Estimation of the number of accumulated AuNPs. (f), SEM images of tiny amounts of printed AuNPs. (g), Fabrication of submicrometer-scaled nanoclusters. The scale bars of Figure 4f,g represent 1 μ m.

The net force marked in the black arrow, consisting of three forces $\vec{F} = \vec{F}_1 + \vec{F}_2 + \vec{F}_3$, explains the creation of a pendant droplet at the tip of the NFP Figure 4a). Because R_2 is significantly smaller than R_1 , the net force can be approximated as $\vec{F} \approx \vec{F}_1 + \vec{F}_3$. Therefore, the sign of the net force is determined by the competition between the capillary force (lifting up) and gravitational force (pulling down), and the filling height (H) of the ink is the main

parameter in this relation. The critical height of the ink ($H_0 \sim 17$ mm) is represented when the net force is in equilibrium, i.e., $F = 0$. If the sign of the net force is positive or H is less than H_0 , the ink is pulled into the nozzle, making contact with the substrate difficult during the contact step (left image in Figure 4a). However, if the sign of the net force is negative or H is larger than H_0 , a pendant droplet is generated at the end of the nozzle, facilitating easier contact (right image in Figure 4a). When a pendant droplet is formed marked in the red dotted circle of Figure 4a, the sign of the curvature of the interface changes, and the direction of F_2 changes upward, which inhibits the growth of the pendant droplet and prevents the ink from leaking. For this reason, we started the stamp-like process by filling more than 20 mm of ink, as shown in Figure 1b.

The volume of the nanocluster is determined from the amount of water evaporated during the first accumulation step of the stamp-like process. Under the contact conditions described above, the water evaporated at the interface of the pendant droplet formed at the end of the NFP nozzle (Figure 4b). The evaporation phenomenon that occurs in spherical water droplets was considered to qualitatively evaluate the amount of evaporation (first image in Figure 4b). Evaporation occurs at the interface of the spherical water droplets because of the difference in the density of water molecules, which can be described by the diffusion equation ($\frac{\partial \tilde{c}}{\partial t} = C_D \nabla^2 \tilde{c}$). Here, $C_D \sim 2.6 \times 10^{-5}$ m²/s is the diffusion constant of vapor in the ambient air, and \tilde{c} is the vapor concentration for water [52]. At small scales in the range of micrometers, this diffusion stabilizes quickly; the left term representing the time variable of the diffusion becomes zero ($\frac{\partial \tilde{c}}{\partial t} = 0$). Therefore, the diffusion equation becomes the well-known Laplace equation ($C_D \nabla^2 \tilde{c} = 0$). To solve this equation, the water vapor is saturated at the water droplet interface ($\tilde{c}_s \sim 19.96$ g/m³), and the water vapor density at a distance from the interface $\tilde{c}_0 \sim 7.99$ g/m³ is required as the boundary condition. The solution of the diffusion equation then becomes $\tilde{c}(r) = \tilde{c}_0 - (\tilde{c}_s - \tilde{c}_0)R/r$ in spherical coordinates, where r is the distance from the center of the droplet, and R is the radius of the droplet. The temperature is 25 °C degrees. The water vapor flux ($\vec{J} = -C_D \nabla \tilde{c}$) can be obtained from the gradient of the water vapor distribution function $\tilde{c}(r)$. By continuously integrating the flux passing through the closed surface enclosing the water droplet, the mass loss rate ($\dot{M} = dM/dt$) can be expressed as $\dot{M} = 1/2 \times \oint \vec{J} \cdot d\vec{a}$, and the volume loss rate ($\dot{V} = \dot{M}/\rho$) of the evaporated water can be obtained. The reason for multiplying 0.5 by $\frac{dM}{dt}$ is that only approximately half of the pendant droplets contribute to evaporation. Thus, the ink flow in the NFP caused by the evaporation of water continued to supply fresh ink to the interface of the pendant droplet. Because of the continuous supply of fresh ink and evaporation, the accumulation of AuNPs occurred at the interface of the pendant droplets, and the amount was proportional to the accumulation time.

The accumulated AuNPs were transferred to the substrate through a capillary bridge (CB) during the contact step. In the second step of the stamp-like process, the pendant droplet made contact with the raised substrate. As the pendant droplet connected to the substrate, it changed into a water column called the CB (Figure 4c). During the formation of the CB, the AuNPs accumulated in the pendant droplet are transferred to the substrate. Simultaneously, the fluid flow due to evaporation occurring at the CB interface rearranged the AuNPs so that they are more distributed at the interface. This transfer and rearrangement process contributed to the nanocluster becoming a half-donut-like shape after detachment (Figure 4d).

The volume of the nanoclusters generated can be analyzed more quantitatively using the volume fraction of AuNPs dispersed in the ink. Because the volume occupied by the AuNPs contained in the ink was minimal, the ink concentration was approximated as a volume fraction expressed as $\tilde{\gamma} \approx \frac{c_{\text{ink}}}{\rho}$. Then, the volume of AuNPs accumulated during the accumulation time (t_A) is expressed as $V_{\text{NP}} = \tilde{\gamma} \dot{V} t_A$, and the volume of the nanocluster formed is expressed as $V_{\text{NC}} = \frac{V_{\text{NP}}}{\gamma}$ because random-close packing of the nanocluster includes void. If V_{NP} is too large in the accumulation stage, the AuNPs cannot transfer fully to the substrate during the contact process, and the remaining AuNPs clog the tip of the NFP nozzle (Figure 4d). This phenomenon is expected to occur when V_{NC} is similar to the

volume of the capillary bridge created between the nozzle tip and the substrate. Therefore, this point was used to divide the clogging and stamping (Figure 4e). The points marked with a cross (+) correspond to the points at which breaking occurred, as indicated by the green box in Figure 2a. Therefore, the separation of clogging and stamping can be fully explained through evaporation-based quantitative analysis.

Notably, even very small nanoclusters can be produced by reducing the accumulation time, ink concentration, and tip inner diameter of the NFP nozzle. In Figure 4e, the black line corresponds to the 138,000 accumulation number of AuNPs, and the conditions of 20 s of accumulation time and 20 mg/mL are also near this line. The radius, 2.5 μm , of the NFP nozzle was used for the calculation. If the accumulation time and radius are reduced to 2 s and 0.25 μm , respectively, then one can expect the accumulation number of AuNPs. For 0.5 and 1 mg/mL of ink concentration, 69 and 138 accumulation numbers were estimated, respectively. This prediction is very similar to the actual experimental results (Figure 4f). The first and second images, in which the number of particles was accurately counted, were similar to the results predicted above, with the number of accumulated AuNPs being 98 and 138, respectively. This result proves that the number of AuNPs created through a stamp-like process can be controlled to 100 by controlling the accumulation time, ink concentration, and NFP nozzle inner diameter. It was possible to repeatedly fabricate submicrometer-level nanoclusters using the diameter of the submicrometer-level NFP nozzle (Figure 4g). The nanocluster manufacturing method developed based on NFP can be easily applied even if the size and composition of the nanoparticles change. In addition, structures can be fabricated using inks mixed with various types of NPs.

Heterogeneous nanoclusters can be easily produced using NFP. Nanoparticles defined as A (green dot) and B (red dot) are evenly mixed according to the second law of thermodynamics (the law of entropy increase) when there is no interaction between them (Figure 5a). Because of this mixed state, A and B are evenly mixed in the structure of the nanoparticles accumulated in the pendant droplet, resulting in the creation of a heterogeneous nanocluster. The mixed state is unaffected by the size and composition of the nanoparticles at a concentration low enough that interactions between nanoparticles do not occur, so the structure of the nanocluster can be more easily tuned. To modulate the structure of the heterogeneous nanocluster, large and small gold and silver nanoparticles were used (Figure 5b). Here, G and g refer to AuNPs (yellow), S and s refer to AgNPs (gray), and upper and lower case letters represent large and small nanoparticles, respectively. When the sizes of AuNPs and AgNPs are similar (GS and gs), they exhibit a random closed packing structure as shown in Figure 5c. On the other hand, when G and s are mixed, the packing structure changes significantly depending on the mixing ratio (Figure 5d). When the ratio of s is low, s is inserted among G, making the void space of the heterogeneous nanocluster. When the ratio of s is large enough ($N_G:N_s = 1:10$ is sufficient.) s encloses G. Here, N represents the number of nanoparticles. And it returns to the random closed packing structure when there is only s. Because this structural change depends only on the size of the nanoparticle, the same structural change occurs in a combination of Gg, Ss, and Sg. The scattering spectra were modulated due to structural changes in the heterogeneous nanocluster (Figure 5e,f), where the spectrum was measured by a dark-field microscope (BX53M, Olympus, Tokyo, Japan) with a spectrometer (USB 2000+, Ocean Insight, Orlando, FL, USA). The spectrum generated by LSPR changed sequentially depending on the composition ratio of the nanoparticles constituting heterogeneous. By mapping the spectral results to the CIE 1931 color space, it was easy to confirm that color changes occur due to structural changes (Figure 5g). Through this method, one can easily explore composition ratios with rapid color changes, and it is expected that this will be useful in developing SERS or LSPR optical devices. We note the diameters for each symbol: G (77 nm), g (15 nm), S (75 nm), and s (25 nm).

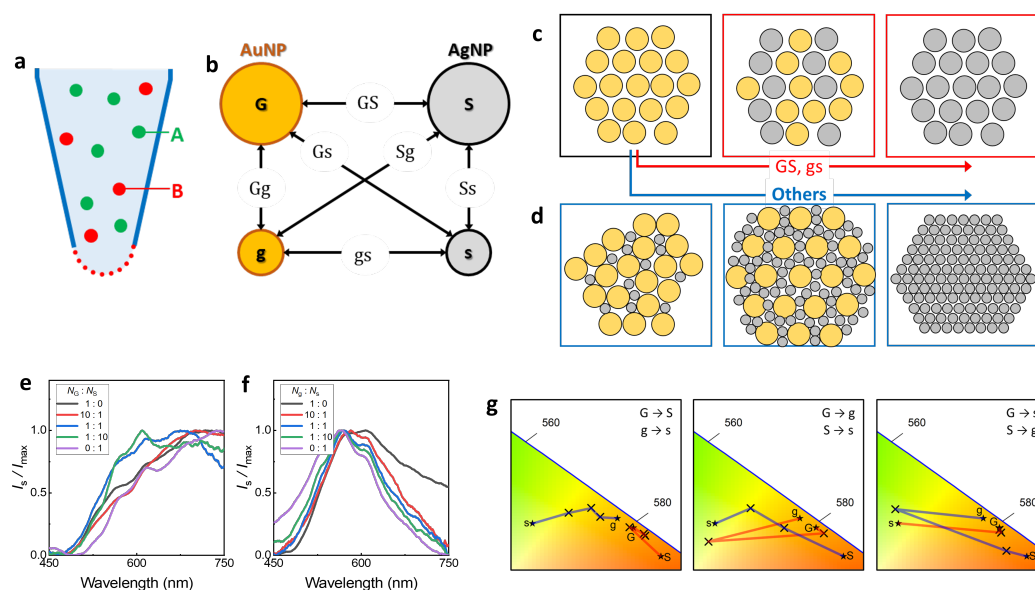


Figure 5. Heterogeneous nanocluster consisting of gold and silver nanoparticles. (a), Schematic of heterogeneous nanocluster fabrication. (b), Combinations of gold and silver nanoparticles regarding size. (c), Mixing of similar-sized nanoparticles. (d), Mixing of small and large nanoparticles. The spectrum of scattered light from heterogeneous nanoclusters for (e) (GS) and (f) (gs). (g), Color shift on the CIE 1931 color space according to mixing ratio.

4. Conclusions

We demonstrate the fabrication and mechanism of a nanofountain pen (NFP)-based nanocluster that operates by balancing the spontaneous evaporation of water and capillary action. By controlling the amount of ink in which the AuNPs are dispersed and filled in the NFP, we found the conditions under which a pendant droplet would form at the end of the nozzle tip and controlled it to enable contact with the substrate in a stamp-like process. In the accumulation step, the ink evaporates from the nozzle tip of the micrometer-level NFP, and AuNPs accumulate at the interface of the pendant droplet. The AuNPs accumulated in the contact step are transferred to the substrate through the capillary bridge (CB), and the fluid flow due to evaporation at the CB interface rearranges the AuNPs, contributing to the nanocluster adopting a half-donut-like shape in the detachment step. By solving the diffusion equation, it was understood that picoliters of ink evaporate per second from the nozzle tip, and hundreds to thousands of AuNPs accumulate at the interface of the pendant droplet. In addition, submicrometer-level nanoclusters can be produced by controlling the accumulation time, ink concentration, and inner diameter of the nozzle. The NFP-based nanocluster fabrication method developed in this study was not limited by the diversity of the NP sizes and compositions and can even be fabricated including metabolites. Therefore, it is expected to be widely applicable to producing two-dimensional and three-dimensional nanostructures and studying the optical properties of surface plasmon resonance or surface-enhanced Raman scattering to develop biosensors for metabolite-based diagnosis.

Author Contributions: Conceptualization, S.-J.K., D.Y., J.-S.M. and J.-W.O.; methodology, S.-J.K. and D.Y.; formal analysis, S.-J.K.; investigation, I.H.L., W.-G.K. and Y.-J.K.; data curation, S.-J.K.; writing—original draft preparation, S.-J.K. and D.Y.; writing—review and editing, S.-J.K., D.Y., J.-S.M. and J.-W.O. All authors have read and agreed to the published version of the manuscript.

Funding: This work was supported by a 2-Year Research Grant of Pusan National University.

Data Availability Statement: The data presented in this study are available in the article.

Conflicts of Interest: The authors declare no conflict of interest.

Abbreviations

The following abbreviations are used in this manuscript:

NP	Nanoparticle
NFP	Nanofountain Pen
CB	Capillary Bridge
SEM	Scanning Electron Microscope
AFM	Atomic Force Microscope
LSPR	Localized Surface Plasmon Resonance
SERS	Surface-enhanced Raman scattering

References

1. Hutter, E.; Fendler, J.H. Exploitation of localized surface plasmon resonance. *Adv. Mater.* **2004**, *16*, 1685–1706. [[CrossRef](#)]
2. Jensen, T.R.; Malinsky, M.D.; Haynes, C.L.; Van Duyne, R.P. Nanosphere lithography: Tunable localized surface plasmon resonance spectra of silver nanoparticles. *J. Phys. Chem.* **2000**, *104*, 10549–10556. [[CrossRef](#)]
3. Ringe, E.; McMahon, J.M.; Sohn, K.; Cogley, C.; Xia, Y.; Huang, J.; Schatz, G.C.; Marks, L.D.; Van Duyne, R.P. Unraveling the effects of size, composition, and substrate on the localized surface plasmon resonance frequencies of gold and silver nanocubes: A systematic single-particle approach. *J. Phys. Chem. C* **2010**, *114*, 12511–12516. [[CrossRef](#)]
4. Mayer, K.M.; Hafner, J.H. Localised surface plasmon resonance sensors. *Chem. Rev.* **2011**, *111*, 3828–3857. [[CrossRef](#)] [[PubMed](#)]
5. Petryayeva, E.; Krull, U.J. Localized surface plasmon resonance: Nanostructures, bioassays and biosensing—A review. *Anal. Chim. Acta* **2011**, *706*, 8–24. [[CrossRef](#)] [[PubMed](#)]
6. Cao, J.; Sun, T.; Grattan, K.T. Gold nanorod-based localized surface plasmon resonance biosensors: A review. *Sens. Actuators B Chem.* **2014**, *195*, 332–351. [[CrossRef](#)]
7. Wu, J.L.; Chen, F.C.; Hsiao, Y.S.; Chien, F.C.; Chen, P.; Kuo, C.H.; Huang, M.H.; Hsu, C.S. Surface plasmonic effects of metallic nanoparticles on the performance of polymer bulk heterojunction solar cells. *ACS Nano* **2011**, *5*, 959–967. [[CrossRef](#)]
8. Du, P.; Jing, P.; Li, D.; Cao, Y.; Liu, Z.; Sun, Z. Plasmonic Ag@ oxide nanoprisms for enhanced performance of organic solar cells. *Small* **2015**, *11*, 2454–2462. [[CrossRef](#)]
9. Lee, H.B.; Kim, W.G.; Lee, M.; Lee, J.M.; He, S.; Kumar, N.; Devaraj, V.; Choi, E.J.; Jeon, I.; Song, M.; et al. Gap Plasmon of Virus-Templated Biohybrid Nanostructures uplifting the performance of organic optoelectronic devices. *Adv. Opt. Mater.* **2020**, *8*, 1902080. [[CrossRef](#)]
10. Xiao, Q.; Jaatinen, E.; Zhu, H. Direct Photocatalysis for Organic Synthesis Using Plasmonic-Metal Nanoparticles Irradiated with Visible Light. *Chem. Asian J.* **2014**, *9*, 3046–3064. [[CrossRef](#)]
11. Kolemen, S.; Ozdemir, T.; Lee, D.; Kim, G.M.; Karatas, T.; Yoon, J.; Akkaya, E.U. Remote-controlled release of singlet oxygen by the plasmonic heating of endoperoxide-modified gold nanorods towards a paradigm change in photodynamic therapy. *Angew. Chem.* **2016**, *128*, 3670–3674. [[CrossRef](#)]
12. Hung, W.H.; Aykol, M.; Valley, D.; Hou, W.; Cronin, S.B. Plasmon resonant enhancement of carbon monoxide catalysis. *Nano Lett. Mater.* **2010**, *10*, 1314–1318. [[CrossRef](#)] [[PubMed](#)]
13. Mao, P.; Liu, C.; Favraud, G.; Chen, Q.; Han, M.; Fratilocchi, A.; Zhang, S. Broadband Single-Molecule SERS Detection Design Using Warped Optical Spaces. *Nat. Commun.* **2018**, *9*, 5428. [[CrossRef](#)] [[PubMed](#)]
14. Kneipp, J.; Kneipp, H.; Kneipp, K. SERS: A single-molecule and nanoscale tool for bioanalytics. *Chem. Soc. Rev.* **2008**, *37*, 1052–1060. [[CrossRef](#)]
15. Alvarez-Puebla, R.A.; Liz-Marzán, L.M. SERS Detection of Small Inorganic Molecules and Ions. *Angew. Chem. Int. Ed.* **2012**, *51*, 11214–11223. [[CrossRef](#)]
16. Sonnefraud, Y.; Verellen, N.; Sobhani, H.; Vandenbosch, G.A.; Moshchalkov, V.V.; Van Dorpe, P.; Nordlander, P.; Maier, S. Experimental realization of subradiant, superradiant, and Fano resonance in ring/disk plasmonic nanocavities. *ACS Nano* **2010**, *4*, 1664–1670. [[CrossRef](#)]
17. Fan, J.A.; Bao, K.; Wu, C.; Bao, J.; Bardhan, R.; Halas, N.J.; Manoharan, V.N.; Shvets, G.; Nordlander, P.; Capasso, F. Fano-like interference in self-assembled plasmonic quadrumer clusters. *Nano Lett.* **2010**, *10*, 4680–4685. [[CrossRef](#)]
18. Shao, T.; Wang, X.; Dong, H.; Liu, S.; Duan, D.; Li, Y.; Song, P.; Jiang, H.; Hou, Z.; Gao, C.; et al. A Stacked Plasmonic Metamaterial with a strong localized electric field enables highly efficient Broadband Light-Driven CO₂ hydrogenation. *Adv. Mater.* **2022**, *34*, 2202367. [[CrossRef](#)]
19. Ji, T.; Peng, L.; Zhu, Y.; Yang, F.; Cui, Y.; Wu, X.; Liu, L.; He, S.; Zhu, F.; Hao, Y. Plasmonic broadband absorber by stacking multiple metallic nanoparticle layers. *Appl. Phys. Lett.* **2015**, *106*, 161107. [[CrossRef](#)]
20. Saeed, A.; Panaro, S.; Zaccaria, R.P.; Raja, W.; Liberale, C.; Dipalo, M.; Messina, G.C.; Wang, H.; De Angelis, F.; Toma, A. Stacked optical antennas for plasmon propagation in a 5 nm-confined cavity. *Sci. Rep.* **2015**, *5*, 11237. [[CrossRef](#)]
21. Kim, W.G.; Lee, J.M.; Yang, Y.; Kim, H.; Devaraj, V.; Kim, M.; Jeong, H.; Choi, E.J.; Yang, J.; Jang, Y.; et al. Three-dimensional plasmonic nanocluster-driven light-matter interaction for photoluminescence enhancement and picomolar-level biosensing. *Nano Lett.* **2022**, *22*, 4702–4711. [[CrossRef](#)] [[PubMed](#)]

22. Zhang, Y.; Zhen, Y.R.; Neumann, O.; Day, J.K.; Nordlander, P.; Halas, N.J. Coherent anti-Stokes Raman scattering with single-molecule sensitivity using plasmonic Fano resonance. *Nat. Commun.* **2014**, *5*, 4424. [[CrossRef](#)] [[PubMed](#)]
23. Chu, M.W.; Myroshnychenko, V.; Chen, C.H.; Deng, J.P.; Mou, C.Y.; García de Abajo, F.J. Probing bright and dark surface-plasmon modes in individual and coupled noble metal nanoparticles using an electron beam. *Nano Lett.* **2009**, *9*, 399–404. [[CrossRef](#)] [[PubMed](#)]
24. Lee, J.; You, E.A.; Hwang, D.W.; Kang, S.; Wi, J.S. Active Accumulation of Spherical analytes on plasmonic hot Spots of Double-Bent Au Strip Arrays by Multiple Dip Coating. *Nanomaterials* **2019**, *9*, 660. [[CrossRef](#)] [[PubMed](#)]
25. Tahghighi, M.; Mannelli, I.; Janner, D.; Ignés-Mullol, J. Tailoring plasmonic Response by Langmuir-Blodgett gold nanoparticle templating for the Fabrication of SERS Substrates. *Appl. Surf. Sci.* **2018**, *447*, 416–422. [[CrossRef](#)]
26. Hanske, C.; Tebbe, M.; Kuttner, C.; Bieber, V.; Tsukruk, V.V.; Chanana, M.; König, T.A.; Fery, A. Strongly coupled plasmonic modes in macroscopic areas via template-assisted colloidal self-assembly. *Nano Lett.* **2014**, *14*, 6863–6871. [[CrossRef](#)]
27. Koster, H.J.; Guillen-Perez, A.; Gomez-Diaz, J.S.; Navas-Moreno, M.; Birkeland, A.C.; Carney, R.P. Fused Raman spectroscopic analysis of blood and saliva delivers high accuracy for head and neck cancer diagnostics. *Sci. Rep.* **2022**, *12*, 18464. [[CrossRef](#)]
28. Schedin, F.; Lidorikis, E.; Lombardo, A.; Kravets, V.G.; Geim, A.K.; Grigorenko, A.N.; Novoselov, K.S.; Ferrari, A.C. Surface-enhanced Raman spectroscopy of graphene. *ACS Nano* **2010**, *4*, 5617–5626. [[CrossRef](#)]
29. Shen, Y.; Yue, J.; Xu, W.; Xu, S. Recent progress of surface-enhanced Raman spectroscopy for subcellular compartment analysis. *Theranostics* **2021**, *11*, 4872. [[CrossRef](#)]
30. Shi, R.; Liu, X.; Ying, Y. Facing challenges in real-life application of surface-enhanced Raman scattering: Design and nanofabrication of surface-enhanced Raman scattering substrates for rapid field test of food contaminants. *J. Agric. Food Chem.* **2017**, *66*, 6525–6543. [[CrossRef](#)]
31. Li, X.; Keshavarz, M.; Kassanos, P.; Kidy, Z.; Roddan, A.; Yeatman, E.; Thompson, A.J. SERS Detection of Breast Cancer-Derived Exosomes Using a Nanostructured Pt-Black Template. *Adv. Sens. Res.* **2023**, *2*, 2200039. [[CrossRef](#)]
32. Kneipp, K.; Wang, Y.; Kneipp, H.; Perelman, L.T.; Itzkan, I.; Dasari, R.R.; Feld, M.S. Single molecule detection using surface-enhanced Raman scattering (SERS). *Phys. Rev. Lett.* **1997**, *78*, 1667. [[CrossRef](#)]
33. Kudelski, A. Analytical applications of Raman spectroscopy. *Talanta* **2008**, *76*, 1–8. [[CrossRef](#)] [[PubMed](#)]
34. Lane, L.A.; Qian, X.; Nie, S. SERS nanoparticles in medicine: from label-free detection to spectroscopic tagging. *Chem. Rev.* **2015**, *115*, 10489–10529. [[CrossRef](#)] [[PubMed](#)]
35. Nie, S.; Emory, S.R. Probing single molecules and single nanoparticles by surface-enhanced Raman scattering. *Science* **1997**, *275*, 1102–1106. [[CrossRef](#)]
36. Yonzon, C.R.; Haynes, C.L.; Zhang, X.; Walsh, J.T.; Van Duyne, R.P. A glucose biosensor based on surface-enhanced Raman scattering: Improved partition layer, temporal stability, reversibility, and resistance to serum protein interference. *Anal. Chem.* **2004**, *76*, 78–85. [[CrossRef](#)]
37. Camden, J.P.; Dieringer, J.A.; Wang, Y.; Masiello, D.J.; Marks, L.D.; Schatz, G.C.; Van Duyne, R.P. Probing the structure of single-molecule surface-enhanced Raman scattering hot spots. *J. Am. Chem. Soc.* **2008**, *130*, 12616–12617. [[CrossRef](#)]
38. Chen, G.; Wang, Y.; Yang, M.; Xu, J.; Goh, S.J.; Pan, M.; Chen, H. Measuring ensemble-averaged surface-enhanced Raman scattering in the hotspots of colloidal nanoparticle dimers and trimers. *J. Am. Chem. Soc.* **2010**, *132*, 3644–3645. [[CrossRef](#)]
39. Le Ru, E.C.; Etchegoin, P.G.; Meyer, M. Enhancement factor distribution around a single surface-enhanced Raman scattering hot spot and its relation to single molecule detection. *J. Chem. Phys.* **2006**, *125*, 204701. [[CrossRef](#)]
40. Premasiri, W.R.; Lee, J.C.; Sauer-Budge, A.; Théberge, R.; Costello, C.E.; Ziegler, L.D. The biochemical origins of the surface-enhanced Raman spectra of bacteria: A metabolomics profiling by SERS. *Anal. Bioanal. Chem.* **2016**, *408*, 4631–4647. [[CrossRef](#)]
41. Ren, Y.F.; Ye, Z.H.; Liu, X.Q.; Xia, W.J.; Yuan, Y.; Zhu, H.Y.; Chen, X.T.; Hou, R.Y.; Cai, H.M.; Li, D.X.; et al. Surface-enhanced Raman spectroscopy-based metabolomics for the discrimination of Keemun black teas coupled with chemometrics. *LWT-Food Sci. Technol.* **2023**, *181*, 114742. [[CrossRef](#)]
42. Xiao, L.; Wang, C.; Dai, C.; Littlepage, L.E.; Li, J.; Schultz, Z.D. Untargeted Tumor Metabolomics with Liquid Chromatography–Surface-Enhanced Raman Spectroscopy. *Angew. Chem.-Int. Edit.* **2020**, *132*, 3467–3471. [[CrossRef](#)]
43. Langer, J.; Jimenez de Aberasturi, D.; Aizpurua, J.; Alvarez-Puebla, R.A.; Auguie, B.; Baumberg, J.J.; Bazan, G.C.; Bell, S.E.; Boisen, A.; Brolo, A.G.; et al. Present and future of surface-enhanced Raman scattering. *ACS Nano* **2019**, *14*, 28–117. [[CrossRef](#)] [[PubMed](#)]
44. Tantra, R.; Brown, R.J.; Milton, M.J. Strategy to improve the reproducibility of colloidal SERS. *J. Raman Spectrosc.* **2007**, *38*, 1469–1479. [[CrossRef](#)]
45. Tripp, R.A.; Dluhy, R.A.; Zhao, Y. Novel nanostructures for SERS biosensing. *Nano Today* **2008**, *3*, 31–37. [[CrossRef](#)]
46. Jang, M.; Shin, J.; Kim, Y.H.; Jeong, T.Y.; Jo, S.; Kim, S.J.; Devaraj, V.; Kang, J.; Choi, E.J.; Lee, J.E.; et al. 3D superstructure based metabolite profiling for glaucoma diagnosis. *Biosens. Bioelectron.* **2023**, *244*, 115780. [[CrossRef](#)]
47. Kim, S.J.; Lee, I.H.; Kim, W.G.; Hwang, Y.H.; Oh, J.W. Fountain-Pen-inspired 3D Colloidal Assembly, Consisting of Metallic Nanoparticles on a Femtoliter Scale. *Nanomaterials* **2023**, *13*, 2403. [[CrossRef](#)]
48. Dullien, F.A. *Porous Media: Fluid Transport and Pore Structure*; Academic press: San Diego, CA, USA, 1992.
49. CVR. *Lange's Handbook of Chemistry*, 10th ed.; McGraw-Hill: New York, NY, USA, 1968; p. 449.
50. Cui, J.; Ju, Y.; Liang, K.; Ejima, H.; Lörcher, S.; Gause, K.T.; Richardson, J.J.; Caruso, F. Nanoscale engineering of low-fouling surfaces through polydopamine immobilization of zwitterionic peptides. *Soft Matter* **2014**, *10*, 2656–2663. [[CrossRef](#)]

-
51. Shuturminska, K.; Tarakina, N.V.; Azevedo, H.S.; Bushby, A.J.; Mata, A.; Anderson, P.; Al-Jawad, M. Elastin-like protein with statherin derived peptides controls fluorapatite formation and morphology. *Front. Physiol.* **2017**, *8*, 368. [[CrossRef](#)]
 52. Cussler, E. L. *Diffusion: Mass Transfer in Fluid Systems*; Cambridge University Press: Cambridge, UK, 2009.

Disclaimer/Publisher's Note: The statements, opinions and data contained in all publications are solely those of the individual author(s) and contributor(s) and not of MDPI and/or the editor(s). MDPI and/or the editor(s) disclaim responsibility for any injury to people or property resulting from any ideas, methods, instructions or products referred to in the content.